Multispectral imaging in the extended near-infrared window based on endogenous chromophores

Qian Cao
Natalia G. Zhegalova
Steven T. Wang
Walter J. Akers
Mikhail Y. Berezin

Multispectral imaging in the extended near-infrared window based on endogenous chromophores

Qian Cao, Natalia G. Zhegalova, Steven T. Wang, Walter J. Akers, and Mikhail Y. Berezin
Washington University School of Medicine, Department of Radiology, St. Louis, Missouri 63110

Abstract. To minimize the problem with scattering in deep tissues while increasing the penetration depth, we explored the feasibility of imaging in the relatively unexplored extended near infrared (exNIR) spectral region at 900 to 1400 nm with endogenous chromophores. This region, also known as the second NIR window, is weakly dominated by absorption from water and lipids and is free from other endogenous chromophores with virtually no autofluorescence. To demonstrate the applicability of the exNIR for bioimaging, we analyzed the optical properties of individual components and biological tissues using an InGaAs spectrophotometer and a multispectral InGaAs scanning imager featuring transmission geometry. Based on the differences in spectral properties of tissues, we utilized ratiometric approaches to extract spectral characteristics from the acquired three-dimensional "datacube". The obtained images of an exNIR transmission through a mouse head revealed sufficient details consistent with anatomical structures. © *2013 Society of Photo-Optical Instrumentation Engineers (SPIE)* [DOI: 10.1117/1.JBO.18.10.101318]

Keywords: extended near infrared; multispectral imaging; endogenous chromophores; water; lipids.

Paper 130119SSPR received Mar. 2, 2013; revised manuscript received May 21, 2013; accepted for publication Jul. 8, 2013; published online Aug. 12, 2013.

1 Introduction

Optical imaging provides a wealth of clinically relevant information regarding the physiological composition of tissues.[1] Changes in optical properties of tissues can reflect pathological alternation and be considered as a marker of a disease. Hence, a variety of approaches centered on interrogating endogenous tissue properties such as scattering, absorption, reflectance, autofluorescence, refractive index, polarization, and exogenous NIR probes has been utilized in biomedical optical imaging.[2–5] The information obtained can be maximized by multispectral capabilities that provide rich information about the individual chromophores and their interactions that contribute to the intensity and location of the optical signal. Multispectral analysis can discriminate intrinsic optical signals that are influenced by functional perturbations or characteristic pathologic changes and have been explored in skin lesions,[6] vascular abnormalities,[7] and cancer.[8–10]

The current state-of-the-art deep tissue and *in vivo* optical imagings are based on endogenous and exogenous optical contrast agents absorbing and/or emitting light in the region 700 to 900 nm known as the near infrared (NIR) optical window.[11] Photon penetration into living tissue is highly dependent on the absorption and scattering properties of tissue components and attenuation is significantly less at wavelengths longer than 700 nm.[12] Thus, the NIR region of the spectrum has been widely utilized in the last decade[3,13] and a number of clinical applications based on NIR imaging have been developed.[14,15] In contrast, the extended NIR (exNIR) optical range of 900 to 1400 nm, known as the second NIR window,[16,17] remains relatively unexplored in biomedical imaging.

The advantage of this region over the NIR range is due to the relative decrease in scattering and increase in transparency of the biological tissue to exNIR light. The Rayleigh scattering of photons in tissue is inversely proportional to the photon's

wavelength ($I \sim \lambda^{-4}$). In the spectral range of 600 to 1500 nm, for many tissues the scattering coefficient decreases with the wavelength in accordance with a power law.[18] Overall, the improvement in the depth penetration for the exNIR spectral range is expected to be substantially larger than in optical window 1 as predicted by several authors[19–21] and which was recently explored with single-wall carbon nanotubes emitting at >1000 nm[16,17,22] and two-photon excitation of NIR fluorescent reporters probes at 1550 nm.[23,24]

Here, we demonstrated that water and lipids dominate the spectral landscape in exNIR by a set of characteristic absorption bands, and we explored the feasibility of imaging in exNIR by focusing on water and lipids as endogenous absorbers. We hypothesized that the position and the relative intensity of the peaks in exNIR are tissue specific and reflect tissue composition. First, we recorded spectra of three major model components in tissue: water, proteins, and lipids. Although some of the optical properties have been published, we have revisited the studies with a new approach by using deuterium oxide (D_2O) as an exNIR transparent solvent and a high resolution spectrophotometer dedicated to exNIR. Having established optical properties of individual components, we recorded spectra of different mouse tissues using an InGaAs hyperspectral imager and modeled the tissue transmission spectra based on two individual components, water and lipids. Finally, we constructed the *in vivo* map of exNIR transmission using a transillumination geometry imaging system for the head of a mouse to reveal contrast-rich features.

2 Materials and Methods

2.1 Materials

MilliQ water, deuterated water (D_2O) (EMD Millipore Corporation, Cambridge Isotope Laboratories, Inc., Tewksbury, Massachusetts), bovine serum albumin (BSA) (Sigma-Aldrich),

---

Address all correspondence to: Mikhail Y. Berezin, Washington University School of Medicine, Department of Radiology, St. Louis, Missouri 63110. Tel: 314-747-0701; Fax: 314-747-5191; E-mail: berezinm@mir.wustl.edu

hemoglobin (Hb from rabbit, Sigma-Aldrich), and lipids (corn oil, purchased at local supermarket) were used without purification. The choice of corn oil was dictated by the similar chemical composition between vegetable oil and animal fat and their similar exNIR absorption spectra. The liquid form of corn oil at room temperature allowed ease of handling the sample. BSA was dried for 1 h at 100°C under the vacuum with the flow of air (loss 12%). Water, BSA, and hemoglobin were dissolved in D_2O at different concentrations. Protein solutions were first mixed in a 50-mL Eppendorf tube, vortexed, observed for particulates, and centrifuged, if necessary, to eliminate the particulates. To ensure complete oxygenation of Hb, D_2O was saturated with air. Direct optical measurements of Hb are challenging and require careful deoxygenation of HbO_2 that will be addressed in the future.

2.2 Optical Measurements

The exNIR spectra of solutions were recorded using a custom built NIR double grating spectrophotometer based on Olis DB620 spercrtophotometer (Olis, Inc., Bogart, Georgia) and equipped with a thermoelectrically cooled to −45°C InGaAs detector (Electro Optical Systems, Inc., Phoenixville, Pennsylvania). A halogen lamp (Ocean Optics, HL-2000) was used as a light source. Quartz cuvettes of different pathlengths (1 to 10 cm) were used to optimize absorbance signal.

Cuvette with D_2O was used as reference for most of the measurements. D_2O is a form of water where the two hydrogen atoms are replaced with the heavier hydrogen isotope deuterium. Although such replacement results in measureable effects on a number of physical properties (i.e., ensity, melting and boiling points, refractive indexes), D_2O contains similar pKa and solvation properties compared to normal water. Due to its similarity, D_2O often substitutes for water as a solvent in nuclear magnetic resonance (NMR) measurements for the structural characterization of proteins.[25] Despite its structural and chemical similarity, D_2O shows strikingly different optical properties in exNIR.[26] In contrast to normal water, D_2O is practically transparent with up to two orders of magnitude lower molar absorptivity (Fig. 1) and therefore, can be used as a solvent.

Corn oil is not soluble in D_2O and therefore an empty cuvette with air was utilized as a reference point. The concentration of the lipids in corn oil was 1.07 M. This concentration was calculated from the average molecular weight of corn oil (MW = 882) obtained from two major components,

triolein and trilinolein at ca. 1:1 ratio and known density $d = 0.95$ g/cm^3.[27]

2.3 Calculations

Molar absorptivities of individual components measured from absorption spectra were converted to absorption attenuation coefficients. Absorption attenuation coefficients of the tissue were calculated from several components provided in Table 1. The derivations of these equations are given below.

The Lambert–Beer law defines that the intensity of light decreases exponentially with depth in the media:

$$I(\lambda) = I_o(\lambda)e^{-\mu_a(\lambda)x}, \tag{1}$$

where λ is the wavelength of measurement, μ_a is the linear absorption attenuation coefficient in cm^{-1}, and x is the pathlength (depth) in centimeters.

From the definition of absorbance (A) as a log ratio of the exiting to incoming light, the following expression relating the absorbance with the attenuation absorption coefficient μ_a can be obtained:

$$A(\lambda) = \log\left[\frac{I_o(\lambda)}{I(\lambda)}\right] = \log\left[\frac{I_o(\lambda)}{I_o(\lambda)e^{-\mu_a(\lambda)x}}\right] = \log[e^{\mu_a(\lambda)x}]. \tag{2}$$

The rearrangement of Eq. (2) gives Eq. (3):

$$A(\lambda) = \mu_a(\lambda)x \log e \approx 0.434\mu_a(\lambda)x. \tag{3}$$

Absorbance can be also expressed as a function of concentration and molar absorptivity:

$$A(\lambda) = \varepsilon(\lambda)Cx, \tag{4}$$

where ε is molar absorptivity (M^{-1} cm^{-1}) and C is the molar concentration (M).

Combining Eqs. (3) and (4), the attenuation factors can be evaluated from experimentally measured molar absorptivities [Eq. (5)]:

$$\mu_a(\lambda) = 2.302\,\varepsilon(\lambda)C. \tag{5}$$

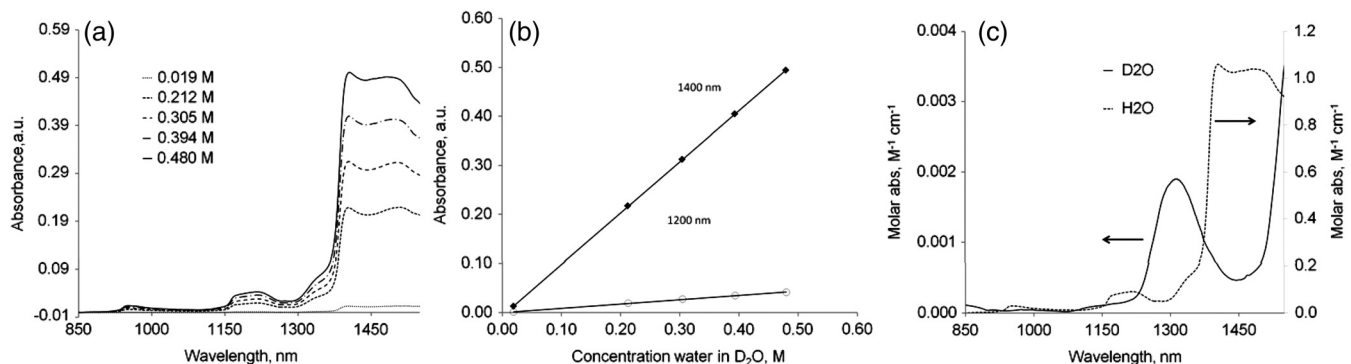The absorptivities of molecular vibrations (see the discussion below) follow Lambert–Beer law similar to electronic

Fig. 1 Absorbance (a) and calibration plot (b) for normal water dissolved in deuterated water D_2O. (b), empty circles: slope at 1200 nm, molar absorptivity $\varepsilon_{1200} = 0.087$ M^{-1} cm^{-1}, $R_2 = 0.999$; solid squares: $\varepsilon_{1400} = 1400$ nm, slope at 1400 nm, molar absorptivity $\varepsilon_{1400} = 1.044$ M^{-1} cm^{-1}, $R_2 = 1$. (c) Molar absorptivity plot of H_2O and D_2O. References: for D_2O spectrum—air; for H_2O spectrum—D_2O. The molar absorptivity spectra of D_2O were recorded using one point of concentration 55.3 M (D_2O) using air as a reference.

Table 1 Tissue composition of various organs based on the compilation of the literature data (Ref. 28).

	Water contents (%)	Lipid contents (%)	Protein contents (%)	Polysaccharides (%)
Whole brain	68.5 to 82.6	5.3 to 18.1	10 to 11.5	—
Adipose[a]	11.4 to 30.5	61.4 to 87.3	7.9	—
Blood	79.0	0.6	19.6	—
Heart	71.0 to 80.9	2.4 to 10.0	15.9 to 18.2	—
Kidney	72.3 to 80.5	2.8 to 6.9	15.8 to 19.9	—
Liver	72.8 to 75.6	1.5 to 7.8	16.1 to 19.6	2.2
Skeletal muscle	70 to 78.6	1.6 to 6.8	17.9 to 21.3	1.0

[a]For adipose in mouse, see Ref. 29.

transitions. Therefore, the intensities of absorption in transmission geometry follow the additivity principle,[30] and hence one can consider the tissue spectra as a sum of different components. From the additivity principle of absorbance, it is possible to demonstrate the additivity of absorption attenuation coefficients [Eq. (6)]:

$$A(\lambda) = \sum_n \varepsilon_n(\lambda)C_n x \quad \text{and} \quad \mu_a(\lambda) = \sum_n \mu_a(\lambda). \quad (6)$$

These sets of equations allow the evaluation of attenuation coefficients from measured absorbance values for a tissue of a known composition. From here, the transmittance of the tissue can be obtained.

$$T(\lambda) = 10^{-A(\lambda)} = 10^{-\sum_n \varepsilon_n(\lambda)C_n x}. \quad (7)$$

2.4 exNIR Imager Design

The imager was assembled for raster scanning in transillumination transmission geometry. The sample (tissue and mouse) was rested on a transparent Petri dish stage supported by two orthogonally overlaying step motors XSlide (Velmex Inc., Bloomfield, New York) (Fig. 2). A 7-W halogen lamp (Ocean Optics, HL-2000) that possesses a relatively broad and stable spectrum in the studied range (900 to 1600 nm) was used to provide illumination. The light was coupled through an NIR optical fiber (Ø1000 μm, 0.39 NA) and into an objective MPLan FMN 10X/0.30 (Olympus) for focusing. The transilluminated light through the sample was captured by another optical fiber (Ø1000 μm, 0.39 NA) and was coupled to a Nunavut InGaAs detector equipped with a high throughput transmission spectrograph, volume-phase grating (VPG) gratings, and an $f/1.8$ design with a range of 800 to 1600 nm. The detector featured a 512-pixel InGaAs array thermoelectrically deep-cooled to $-60°C$ with a resolution of ~1.6 nm/pixel (Bayspec Inc., San Jose, California). During image acquisition, each step movement was accompanied by a full spectral acquisition resulting in a three-dimensional "data-cube", with two spatial dimensions and a spectral dimension. For spectral characterization, the stage was held still, and the integration time of the spectrometer was adjusted to achieve adequate tradeoff between photon count and scan time. For a planar sample, a spatial resolution of ca.

2 mm was measured for small fonts on a printing paper. The actual resolution during scans was expected to be lower due to scattering and absorption in thick tissue. This results in varying resolutions with different samples.

Optical imaging was performed in transillumination geometry as depicted in Fig. 2 by raster scanning as described above. Light was collected on the opposite side (transillumination) via an optical fiber connected to the InGaAs array detector. The integration time of the imager was adjusted to achieve an adequate tradeoff between photon counts and scan time for each location. Images were constructed from spectra as 1 location = 1 pixel. An entire spectrum was collected for each location. Post-processing of acquired data was performed to construct single-wavelength transmission image maps and represented the significant information from each pixel.

2.5 Tissue and Animal Study

Animal studies were conducted in accordance with protocols approved by the Washington University School of Medicine Animal Studies Group and according to the Animal Welfare Act for use of animals in research. One 12-week old female nude mouse was anesthetized (isoflurane, 2% vol/vol) and euthanized by cervical dislocation followed by decapitation. Digital
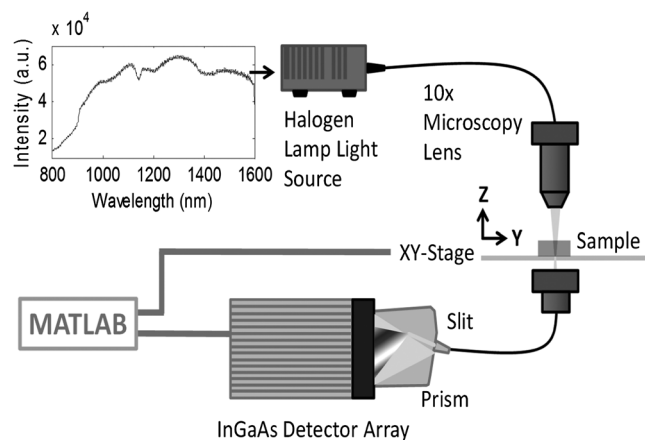

Fig. 2 Experimental imaging setup in 800 to 1600 nm. The spectrum of the halogen lamp in exNIR obtained by this imager is shown in the upper left corner.

radiographs of the head were acquired before the decapitation using the In-Vivo Multispectral FX Pro (Bruker Biospin, Woodbridge, CT). Acquisition time was 90 s using 35 kVp, 149 μA and 0.4 mm filter (12.9 KeV). Specific organs and tissues were harvested from a male mouse and placed on the exNIR imager for detailed spectral characterization.

2.6 Data Analysis

Each spectrum was processed with a fifth order Butterworth low-pass filter with a normalized cutoff frequency of 0.3, determined empirically to remove electronic noise from the detector, which was necessary for quantitative analysis. The resulting transmission spectra were divided by the illumination spectrum and normalized to their respective intensities at 800 nm. For interpolation, a piecewise cubic Hermite method implemented by MATLAB's *interp1* function was used. Modeling of the adipose tissue transmission spectra obtained with a home-made imager was performed from linear combination of water and corn oil spectra obtained using a spectrophotometer (Olis).

3 Results and Discussion

3.1 Molar Absorptivities of Tissue Components in exNIR

Understanding optical properties of a biological tissue in exNIR requires establishing basic optical parameters such as molar absorptivities and absorption coefficients of major tissue components, including water, hemoglobins, proteins, lipids, and carbohydrates. However, measuring molar absorptivities of water and water soluble proteins in the exNIR spectral range is challenging. Water absorbs at wavelengths >1000 nm, with molar absorptivity exceeding 1 M^{-1} cm^{-1} > 1300 nm. Given the very high concentration of pure water ~55.5 M, accurate measurements of molar absorptivities in water would require a cuvette with a < 0.2 mm path length, which is technically demanding. Because of the high water concentration, measuring the absorbance of proteins in water in such a cuvette would be impossible given the submillimolar concentration of proteins even at their highest concentrations (BSA solubility limit in water is 5% wt/vol which is equal to 0.75 mM).

To address this problem, we utilized deuterium oxide (D_2O) as a solvent (see methods). For H_2O molar absorptivity measurements, different amounts of water were added to a cuvette with D_2O, and a calibration curve was generated [Fig. 1(a) and 1(b)].

The molar absorptivity spectrum of normal water and D_2O is shown in Fig. 1(c). The spectrum shows several characteristic peaks at 975 and 1200 nm and exhibits strong absorbance after 1400 nm.

Similarly, the absorption of the proteins HbO_2 and BSA, two major proteins in blood, is recorded in D_2O. Low molar absorptivity of D_2O allows the use of longer path length cuvettes for measuring molar absorptivities of relatively low concentration proteins. Hence, in order to maximize the absorbance of proteins, a 10-cm cuvette was utilized. Measured molar absorptivities for each of the proteins are given in Fig. 3(a) and 3(b). Calculated absorption coefficients μ_a in log scale are provided in Fig. 4. Interestingly, the spectrum of commercial BSA (66 kDa protein) resembled the spectrum of water (not shown), apparently because of incorporated water in the commercial sample (upon drying at ~100°C, the loss of water in protein mass was 12%). Hemoglobin, which is also a protein of a similar size as BSA (64 kDa), shows a much different spectrum with a strong and broad absorption band over the whole range of exNIR due to the presence of heme.

Lipids show relatively low absorbance and can be measured without a dilution matrix in a 3.4-mm quartz cuvette. The absorbance spectra of corn oil reveals several prominent, and more importantly, nonoverlapping peaks with individual features Fig. 3(c). These are located at two major peaks at 1200 and 1380 nm and two valleys at ~1100 and 1300 nm. The most notable comparison to the water spectrum is the absence of a peak at 975 nm. The importance of this peak in image analysis is provided below.

Based on experimentally measured molar absorptivities, the absorption coefficients were calculated using Eq. (5) (Fig. 4).

3.2 Optical Properties of Tissues

Having established the difference between the spectra of individual chromophores, we recorded the spectra of several biological tissues. The spectra were obtained in transmission geometry using the exNIR imager (see methods) and shown in Fig. 5. Each spectrum was constructed as an average from five different points. Most of the organs show bands at 975, 1100, and 1280 nm corresponding to water signals, several smaller peaks, and shoulders originated from the presence of lipids, proteins, and other tissue components. Comparison of the tissue spectral properties with their contents (Table 1) shows a significant level of correlation. Similar correlation between spectral
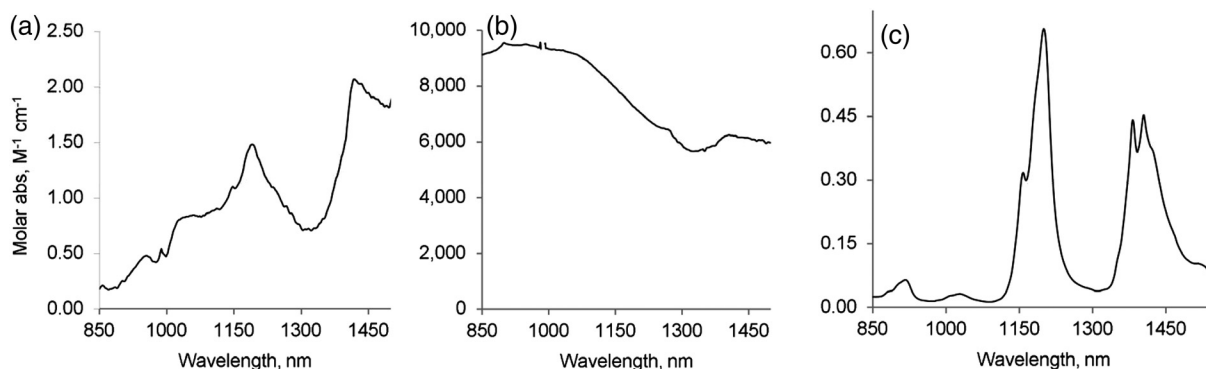

Fig. 3 (a) Molar absorptivity spectrum of BSA after drying in D_2O (cuvette 10 cm, quartz); Reference spectrum—D_2O.(b) molar absorptivity spectrum of hemoglobin in D_2O (cuvette 10 cm, quartz); Reference spectrum—D_2O.(c) molar absorptivity spectrum of corn oil (cuvette 1 cm, quartz); Reference spectrum—air.
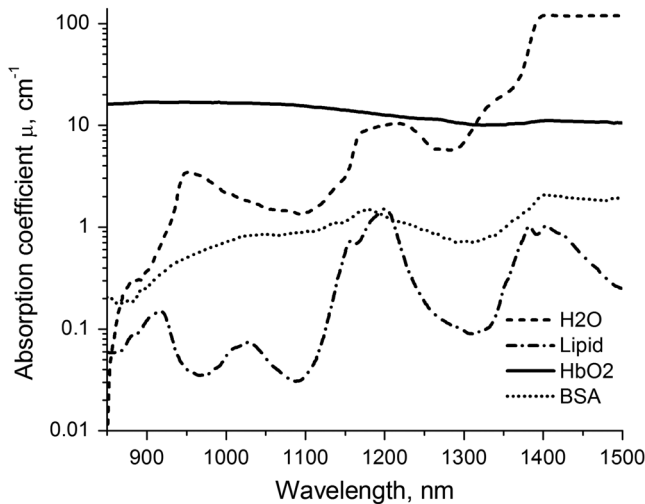
Fig. 4 Absorption coefficients (μ_a) of individual components: water, solutions of hemoglobin, bovine serum albumin (both at 2.5% in D_2O), and lipids.

properties of organs in exNIR and lipid-water composition has been observed previously.[18,31,32] High water-content organs such as blood, kidney, and skeletal muscle share similar bands with different shapes apparently affected by different types of lipids as well as the presence of proteins and other biologically relevant components. Tissues with a high lipid level such as adipose tissue showed the stronger presence of lipid spectral features. Decomposition of the adipose spectra into water and lipid components with 19% water and 81% lipid revealed a high degree of correlation while preserving fine features (Fig. 6).

3.3 Imaging of the Mouse Head

Multispectral exNIR imaging of a mouse head in transillumination geometry was performed for the range 800 to 1400 nm at each data point in the square matrix, creating a $90 \times 65 \times 512$ datacube. The relatively long integration time of 500 ms was
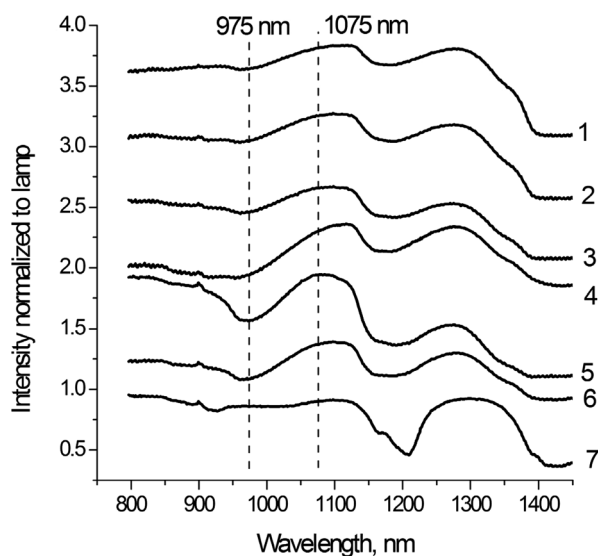

Fig. 5 Spectral characterization of various tissues using an exNIR imager. From top to bottom: 1. skeletal muscle, 2. liver, 3. kidney, 4. cardiac tissue, 5. cerebrum, 6. cerebellum, and 7. adipose. The individual graphs were offset for clarity.

dictated by the use of a low power halogen lamp for illumination and a detector small slit (25 μm) that provided sufficient spectral resolution of 1.6 m/pixel, allowing the selection of individual wavelengths for data processing.

The resulting images produced using the ratio of intensities at 1075 to 975 nm are shown in Fig. 7. A band at 975 nm is a characteristic absorption peak of water, whereas 1075 nm is where the transmission of the tissue is the highest. Both cerebrum and cerebellum tissues show distinguishing spectral features at these two wavelengths (Fig. 5). At 1075/975, the cranial features of the mouse were highlighted with high pixel values in the nasal, premaxilla, maxilla, and orbital areas of the skull (Fig. 7a). Contents of the cranial cavity also seem to be visible to some degree, with three areas of lower intensity which possibly correspond to the cerebral hemispheres and the cerebellum. An X-ray scan of the mouse head (Fig. 7(b)) provided reference of skeletal structures for co-registration of anatomy with exNIR ratio image shown in Fig. 7(c).

4 Discussion

Imaging in the exNIR has been initially limited due to the lack of available optical instrumentation. Commonly utilized silicon-based detectors are inefficient beyond 900 nm resulting in low signals and poor signal-to-noise ratio. Detectors based on germanium (Ge), indium gallium arsenide (InGaAs), indium antimonide (InSb), and mercury cadmium telluride (HgCdTe) are significantly higher in sensitivity in the exNIR range. Out of these detectors, InGaAs with its high quantum efficiency in 900 to 1600 nm has proved to be the most practical for imaging applications.[33] Since a two-dimensional InGaAs camera with satisfactory quantum efficiency did not exist when the project started, the data acquisition was performed with a diode array 1×512 pixel multispectral InGaAs camera synchronized with an XY scanning platform.

The major endogenous chromophore in biological tissue within visible and NIR wavelengths is hemoglobin in its oxygenated (HbO_2) and deoxygenated forms (Hb).[34] At wavelengths longer than 950 nm, the molar absorptivity of HbO_2 predominates.[35,36] Since, in general, the arterial oxygen saturation in adults is >95%,[37] and venous oxygen saturation is 60% to 70%,[38] the spectral properties of blood in exNIR are expected to be defined by the absorption of HbO_2. The spectrum of HbO_2
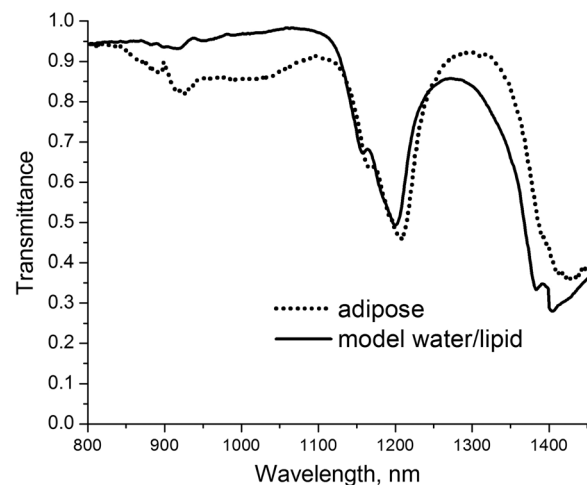

Fig. 6 Modeling adipose tissue by linearly combining spectra of water (19%), and lipid (81%) results in the spectrum similar to the spectrum of adipose acquired from an exNIR image.
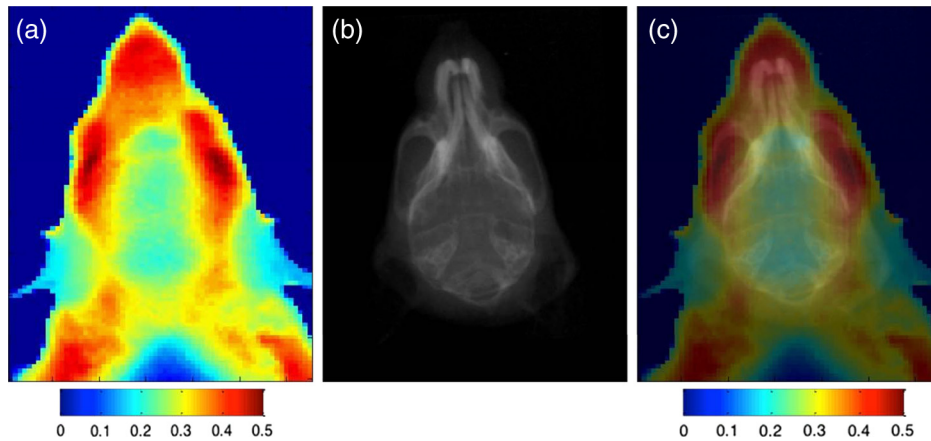
Fig. 7 Imaging of a mouse head (a) exNIR image at the ratio 1075/975 nm, (b) an X-ray image of the same region of the mouse, and (c) coregistration exNIR/X-ray imaging.

up to 1400 nm is structureless with no prominent bands, as demonstrated in this work, and also observed in Ref. 36. Therefore, the absorption of hemoglobin in the exNIR optical range can be considered as background spectra.

Compared with the visible and NIR range where hemoglobins are the dominant absorbers, exNIR provides a different set of dominant chromophores.[36] Above 950 nm, relatively strong absorption signals due to water and lipids become important contributors to tissue absorption.[31,39,40] Water displays characteristic absorption bands at ~970, 1200 and >1400 nm, while lipids exhibited unique bands at 930, 1040, 1210, and 1390 nm (Figs. 1–4). The absorption bands in the spectra are due to mostly water and lipids' overtones and combination bands of their corresponding vibrations (tones).[41,42] The overall water–lipid profile of the tissue absorption in exNIR is characteristic of the type of the tissue, gender, and age [1,43] and might be considered as an optical signature of the tissue.

As water is one of the major contributors to the exNIR spectra profile, its spectra is modulated by the presence of proteins, ions, and other dissolved molecules. Thus, it provides information about the composition of the sample and its environment. The majority of the water molecules in the tissue are hydrogen bonded to biomolecules and ions in the forms of solvated complexes. The addition of organic molecules and ions has shown to cause a noticeable shift (peak position and the intensity) in water's exNIR spectrum. Stronger hydrogen bonding affects the position of the O–H stretching band by shifting it to longer wavelengths and reduces the O–H vibration antiharmonicity (making the effective mass of hydrogen larger) leading to a decrease in signal intensity. Similar to water, lipids' vibrational bands are also expected to reflect the environment. Moreover, significant diversity among lipids (different fatty acids, sterols, phospholipids) will also be reflected by the position and intensity of the bands. Thus, the spectral sensitivity of exNIR active molecules to the environment could be considered as a potential marker of tissue composition in imaging. Due to the low intensity of absorption from the overtones, the absence of other chromophores, no autofluorescence, attenuated scattering, and the sensitivity of the absorption signals to the environment, this exNIR spectral range is an attractive range for imaging.

5 Conclusions

Herein, we demonstrated that multispectral imaging in the exNIR spectral range provides new possibilities in label-free imaging of small animals. Such imaging depends on two major endogenous chromophores in animal tissue, water, and lipids and is capitalized on attenuated scattering in deep tissues. The position and the intensity of the chromophores' spectral bands depend on the tissue composition and thus allow the potential anatomical resolution of the tissue. Based on the differences in exNIR optical properties of tissues, we developed ratiometric techniques for processing the acquired three-dimensional datacube. With this method, the obtained images of a mouse head revealed sufficient resolution and anatomical structures consistent with the anatomy of the mouse head. Further work is needed to more fully elucidate individual molecular signatures and their correlation with the biological functions. Although this study is focused on transmission properties of tissue, our findings open up a new opportunity for developing fluorescent based contrast agents. We envision that a number of such fluorescent probes from single wall nanotubes (SWNT) to quantum dots and upconverted nanoparticles optically active in exNIR can be utilized to enhance the contrast.

References

1. A. Sakudo et al., "Visible and near-infrared spectral changes in the thumb of patients with chronic fatigue syndrome," *Clin. Chim. Acta* **403**(1–2), 163–166 (2009).
2. R. L. van Veen, W. Verkruysse, and H. J. Sterenborg, "Diffuse-reflectance spectroscopy from 500 to 1060 nm by correction for inhomogeneously distributed absorbers," *Opt. Lett.* **27**(4), 246–248 (2002).
3. S. Achilefu et al., "Novel receptor-targeted fluorescent contrast agents for in vivo tumor imaging," *Invest. Radiol.* **35**(8), 479–485 (2000).
4. R. S. Gurjar et al., "Imaging human epithelial properties with polarized light-scattering spectroscopy," *Nat. Med.* **7**(11), 1245–1248 (2001).
5. Z. Wang et al., "Tissue refractive index as marker of disease," *J. Biomed. Opt.* **16**(11), 116017 (2011).

6. M. S. Chin et al., "Hyperspectral imaging for early detection of oxygenation and perfusion changes in irradiated skin," *J. Biomed. Opt.* **17**(2), 026010 (2012).

7. A. Vogel et al., "Using noninvasive multispectral imaging to quantitatively assess tissue vasculature," *J. Biomed. Opt.* **12**(5), 051604 (2007).

8. H. Akbari et al., "Hyperspectral imaging and quantitative analysis for prostate cancer detection," *J. Biomed. Opt.* **17**(7), 076005 (2012).

9. L. Qiu et al., "Multispectral scanning during endoscopy guides biopsy of dysplasia in Barrett's esophagus," *Nat. Med.* **16**(5), 603–606 (2010).

10. A. Cerussi et al., "*In vivo* absorption, scattering, and physiologic properties of 58 malignant breast tumors determined by broadband diffuse optical spectroscopy," *J. Biomed. Opt.* **11**(4), 044005 (2006).

11. V. Ntziachristos, C. Bremer, and R. Weissleder, "Fluorescence imaging with near-infrared light: new technological advances that enable *in vivo* molecular imaging," *Eur. Radiol.* **13**(1), 195–208 (2003).

12. J. R. Mourant et al., "Predictions and measurements of scattering and absorption over broad wavelength ranges in tissue phantoms," *Appl. Opt.* **36**(4), 949–957 (1997).

13. R. Weissleder, "A clearer vision for in vivo imaging," *Nat. Biotechnol.* **19**(4), 316–317 (2001).

14. E. M. Sevick-Muraca, "Translation of near-infrared fluorescence imaging technologies: emerging clinical applications," *Annu. Rev. Med.* **63**, 217–231 (2012).

15. B. E. Schaafsma et al., "The clinical use of indocyanine green as a near-infrared fluorescent contrast agent for image-guided oncologic surgery," *J. Surg. Oncol.* **104**(3), 323–332 (2011).

16. K. Welsher, S. P. Sherlock, and H. J. Dai, "Deep-tissue anatomical imaging of mice using carbon nanotube fluorophores in the second near-infrared window," *Proc. Natl. Acad. Sci. U.S.A.* **108**(22), 8943–8948 (2011).

17. A. M. Smith, M. C. Mancini, and S. Nie, "Bioimaging: second window for in vivo imaging," *Nat. Nanotechnol.* **4**(11), 710–711 (2009).

18. A. N. Bashkatov et al., "Optical properties of human skin, subcutaneous and mucous tissues in the wavelength range from 400 to 2000 nm," *J. Phys. D: Appl. Phys.* **38**(15), 2543 (2005).

19. K. Welsher et al., "A route to brightly fluorescent carbon nanotubes for near-infrared imaging in mice," *Nat. Nanotechnol.* **4**(11), 773–780 (2009).

20. D. Kobat et al., "Deep tissue multiphoton microscopy using longer wavelength excitation," *Opt. Express* **17**(16), 13354–13364 (2009).

21. S. Chitchian and N. M. Fried, "Near-IR optical properties of canine prostate tissue using oblique-incidence reflectometry," *Proc. SPIE* **7548**, 75480Z (2010).

22. H. J. Yi et al., "M13 phage-functionalized single-walled carbon nanotubes as nanoprobes for second near-infrared window fluorescence imaging of targeted tumors," *Nano Lett.* **12**(3), 1176–1183 (2012).

23. M. Y. Berezin et al., "Two-photon optical properties of near-infrared dyes at 1.55 mum excitation," *J. Phys. Chem. B* **115**(39), 11530–11535 (2011).

24. S. Yazdanfar et al., "Multiphoton microscopy with near infrared contrast agents," *J. Biomed. Opt.* **15**(3), 030505 (2010).

25. J. Cavanagh, *Protein NMR Spectroscopy: Principles and Practice*, Academic Press, San Jose, California (2007).

26. V. Lesnyak et al., "One-pot aqueous synthesis of high quality near infrared emitting Cd1-xHgxTe nanocrystals," *J. Mater. Chem.* **19**(48), 9147–9152 (2009).

27. F. D. Gunstone, J. L. Harwood, and A. J. Dijkstra, *The lipid handbook with CD-ROM*, CRC Press, Boca Raton (2007).

28. H. Q. Woodard and D. R. White, "The composition of body tissues," *Br. J. Radiol.* **59**(708), 1209–1218 (1986).

29. L. W. Thomas, "The chemical composition of adipose tissue of man and mice," *Q. J. Exp. Physiol. Cogn. Med. Sci.* **47**(2), 179–188 (1962).

30. B. l. G. Lipták, *Analytical Instrumentation*, Chilton, Radnor, PA (1994).

31. R. Nachabé et al., "Diagnosis of breast cancer using diffuse optical spectroscopy from 500 to 1600 nm: comparison of classification methods," *J. Biomed. Opt.* **16**(8), 087010 (2011).

32. R. Nachabe et al., "Estimation of lipid and water concentrations in scattering media with diffuse optical spectroscopy from 900 to 1,600 nm," *J. Biomed. Opt.* **15**(3), 037015 (2010).

33. M. P. Hansen and D. S. Malchow, "Overview of SWIR detectors, cameras, and applications," *Proc. SPIE* **6939**, 69390I (2008).

34. W. Zijlstra, A. Buursma, and W. Meeuwsen-Van der Roest, "Absorption spectra of human fetal and adult oxyhemoglobin, de-oxyhemoglobin, carboxyhemoglobin, and methemoglobin," *Clin. Chem.* **37**(9), 1633–1638 (1991).

35. S. Prahl, "Optical absorption of hemoglobin," http://omlc.ogi.edu/spectra/hemoglobin/index.html (21 July 2013).

36. R. Nachabe et al., "Estimation of biological chromophores using diffuse optical spectroscopy: benefit of extending the UV-VIS wavelength range to include 1000 to 1600 nm," *Biomed. Opt. Express* **1**(5), 1432–1442 (2010).

37. A. Zourabian et al., "Trans-abdominal monitoring of fetal arterial blood oxygenation using pulse oximetry," *J. Biomed. Opt.* **5**(4), 391–405 (2000).

38. T. Hamaoka et al., "Quantification of ischemic muscle deoxygenation by near infrared time-resolved spectroscopy," *J. Biomed. Opt.* **5**(1), 102–105 (2000).

39. R. L. P. van Veen et al., "Determination of visible near-IR absorption coefficients of mammalian fat using time- and spatially resolved diffuse reflectance and transmission spectroscopy," *J. Biomed. Opt.* **10**(5), 054004 (2005).

40. H. R. Jalian and M. M. Avram, "Body contouring: the skinny on non-invasive fat removal," *Semin. Cutan. Med. Surg.* **31**(2), 121–125 (2012).

41. K. Nakamoto, *Infrared and Raman spectra of inorganic and co-ordination compounds*, Wiley, Hoboken, New Jersey (2009).

42. S. Šašić and Y. Ozaki, *Raman, Infrared, and Near-Infrared Chemical Imaging*, Wiley, Hoboken, NJ (2010).

43. T. J. Allen et al., "Spectroscopic photoacoustic imaging of lipid-rich plaques in the human aorta in the 740 to 1400 nm wavelength range," *J. Biomed. Opt.* **17**(6), 061209 (2012).